Journal of Marine Science and Technology, Vol. 23, No. 5, pp. 761-773 (2015)
DOI: 10.6119/JMST-015-0617-1

NUMERICAL STUDY OF FLOW PAST TWO COUNTER ROTATING CYLINDERS USING IMMERSED BOUNDARY METHOD

Ming-Jyh Chern[1, 2], Farida Rehmawati Purnadiana[1], Dedy Zulhidayat Noor[3], Tzyy-Leng Horng[4], Shiu-Wu Chau[5], and Ernest Odhiambo[1]

Key words: immersed boundary method, rotating cylinder, side-by-side, vortex shedding.

ABSTRACT

The adoption of a direct forcing immersed boundary numerical method on the uniform flow, at a moderate Reynolds number of 100, past a pair of two rotating circular cylinders placed side-by-side, is the core of the present study. A simplified yet novel approach is used to impose a virtual force as a source to the full incompressible two-dimensional Navier-Stokes equations, which are discretized by the finite volume method. The usage of a Cartesian grid that ensures minimal computational cost, is the salient feature of the applied immersed boundary approach. The gap between the two cylinders, and their rotational direction and speed, are the variable parameters used in the analysis of the resulting vortex street. A range of absolute rotational speeds ($|\alpha| \le 3$) for different gap spacings ($g^* \le 3$), is considered. Whilst the direction of rotational motion is found to either accelerate or decelerate the gap flow, the rotational speed has a bearing on the dominant flow pattern. An observation of the vorticity contours for the decelerating gap flow indicates that when a critical rotational speed ($\alpha \approx 1.4$) is reached, the flow becomes steady regardless of the variation of g^*. Five α-dependent flow modes emerge; the anti-phase, in-phase, flip-flop, single vortex shedding and suppressed modes. A statistical scrutiny of the validated transient data for the lift ($\overline{C_L}$) and drag ($\overline{C_D}$) coefficients is ultimately performed. When $g^* = 0.2$, the general trend of decreasing $\overline{C_D}$ with reduction in gap size is broken.

I. INTRODUCTION

Despite the rather unsophisticated nature of cylindrical structures associated with offshore platforms, chimney stacks and buildings, the complexity with which fluids flow around these, and similar installations, has invited a myriad of attention from engineers and scientists alike. Whereas the study of flow past a single stationary cylinder might be regarded as having been exhaustively dealt with, the investigation of flow around an array of grouped rotating cylinders sitting side-by-side is fast gaining prominence. Such focus has not been limited to mere fascination, but has taken on a more serious tone, that of resolving the frequent failures arising from excessive hydrodynamic loading on these structures. The generation and evolution of vortices behind the cylinders will inevitably enhance acoustic noises and vibrations (Kang and Choi, 1999). A case in point is the Flettner ship, which relies on a forward thrust generated by wind flowing past two rotating cylinders, instead of that produced by sails. Although the production of these vessels has largely been dormant for decades now, their revival appears plausible, given the recent technological developments. These advances have gradually enabled the better understanding of key causes of vibrations that lead to the failure of the rotating cylindrical structures on the Flettner ship and other similar vessels. The difficulty of understanding the interaction of the three regions existing around bluff bodies, i.e., the boundary layer, shear layer and wake area, is a major impediment towards research efforts. Thus any attempt towards unraveling these interactions are a boon.

It is well known that the wake characteristics behind two cylinders placed side-by-side depend on the gap, g^* (which is the gap spacing g, normalized by the cylindrical diameter D), between them. Zdravkovich (1982) experimentally studied the flow characteristics of two such cylinders at the Reynolds

Paper submitted 09/24/14; revised 06/03/15; accepted 06/17/15. Author for correspondence: Ming-Jyh Chern (e-mail: mjchern@mail.ntust.edu.tw).
[1] *Department of Mechanical Engineering, National Taiwan University of Science and Technology, Taipei, Taiwan, R.O.C.*
[2] *Ocean Technology Research Center, National Taiwan University, Taipei, Taiwan, R.O.C.*
[3] *Department of Mechanical Engineering Institut Teknologi Sepuluh Nopember, Surabaya, Indonesia.*
[4] *Department of Applied Mathematics, Feng-Chia University, Taichung, Taiwan, R.O.C.*
[5] *Department of Engineering Science Ocean Engineering, National Taiwan University, Taipei, Taiwan, R.O.C.*

number 1000. He categorized flow regimes into three primary patterns. Firstly, a single body pattern in which a single vortex street occurred was observed for $g^* < 0.2$. Next, a biased gap pattern appeared in the range $0.2 \le g^* \le 1$. It was found that two distinctive wakes influenced each other in the gap. Their sizes intermittently changed. Bearman and Weadcock (1973) found that the cylinder with a narrow wake exhibited the higher drag and frequency of vortex shedding. The last one was a coupled vortex street pattern appearing in the range $1 \le g^* \le 3$. Two identifiably different vortex streets either in anti-phase or in-phase synchronized wake patterns were found behind the two cylinders in this range. Bearman and Weadcock (1973) also indicated that the combined drag on those two cylinders was more than double that on a single cylinder in a uniform flow.

In contrast with the experiments, the numerical analyses has far fewer references. Recently, Kang (2003) numerically investigated the characteristics of flow over two side-by-side circular cylinders in the range of low Reynolds number ($40 \le \mathrm{Re} \le 160$) defined as $\mathrm{Re} = U_\infty D/\nu$ where U_∞ and ν are the free stream speed and kinematic viscosity, respectively. For $g^* < 5$, he identified six kinds of wake patterns; the anti-phase-synchronized ($g^* \ge 2$), in-phase-synchronized ($g^* \ge 1.5$), flip-flopping ($0.4 \le g^* \le 1.5$), single-bluff body ($g^* \le 0.4$), deflected ($50 \le \mathrm{Re} \le 110$ and $0.2 \le g^* \le 1.0$) and steady ($\mathrm{Re} \le 40$ and $g^* \ge 0.5$) patterns. These wake patterns, along with the drag and lift coefficients, were illustrated in detail.

The effect of gap size on two stationary cylinders in a side by side arrangement has been well documented (Meneghini et al. (2001) and Kang (2003)). Nevertheless, only a few researchers have considered the effect of rotating cylinders on a fluid flow. Guo et al. (2009) performed particle image velocimetry (PIV) measurements to analyze the modification of flow by the combined effects of rotation and Reynolds number for $g^* = 0.11$ in a flow past two rotating side-by-side cylinders. Considering flows at various Reynolds numbers from 425 to 1130 and dimensionless rotational speeds α of 0 to 4, they found that the mechanism for the suppression of vortex shedding behind two rotating cylinders was very different from that behind a single rotating cylinder. In the case of flow past a rotating cylinder, the separation points are not aligned to the upper and lower surfaces of the cylinder when the vortex shedding is suppressed. The alignment is observed for flow past two rotating side-by-side cylinders. As the rotational speed increased, the separation phenomenon in the boundary layers disappeared. The critical rotational speed and attachment rotational speed decreased with increase in the Reynolds number.

Recently, Yoon et al. (2009) also numerically investigated flow past two rotating side-by-side cylinders using an interpolative immersed boundary method, at various rotational speeds, $\alpha < 2$, for $g^* = 0.2$, 0.7, 1.5 and 3 and Reynolds number 100. Their study showed that the direction of rotation resulted in a decelerating gap flow. As a result, the effect of rotational speed significantly reduced the drag coefficient and

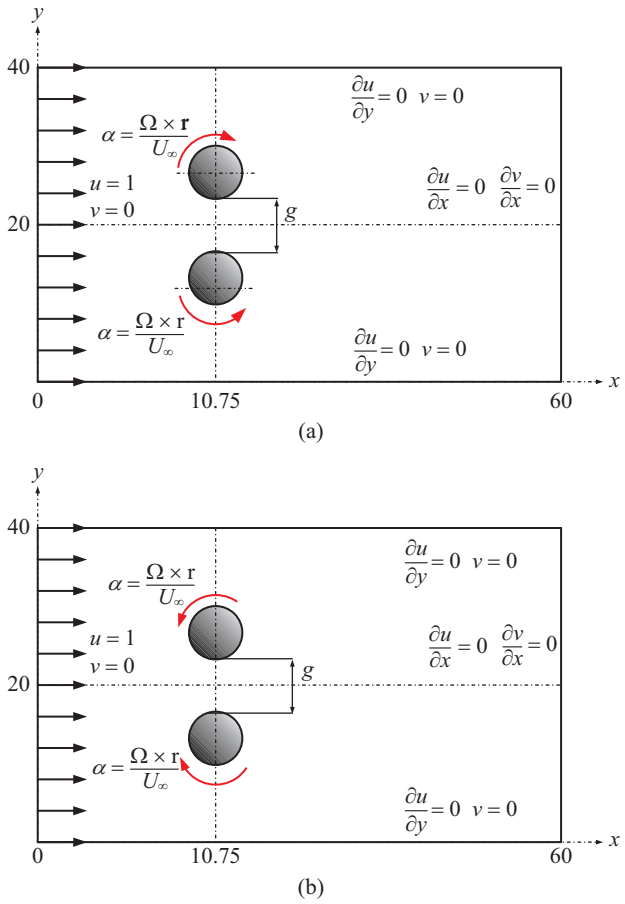

Fig. 1. Schematics of the problems: (a) decelerating gap flow and (b) accelerating gap flow.

suppressed the vortex shedding behind the two cylinders. The vortices adjacent to the gap were seen to be suppressed for higher values of α.

This study attempts to investigate the physical phenomena of a uniform flow past two side-by-side cylinders which rotate in clockwise and counter-clockwise directions. Flow characteristics due to various gaps and rotational speeds are simulated. Practically all the aforementioned numerical studies would have been accomplished by way of a tedious body-conforming mesh generation method. This costly element of the computations is eliminated by the application of a proposed immersed boundary method devoid of numerical complexities. Quantitative and qualitative information about the flow characteristics such as instantaneous contours of vorticity, the drag and lift coefficients are all numerically predicted.

II. PROBLEM DESCRIPTION AND SOLUTION SCHEMES

Fig. 1 shows schematics of the problems considered in this study. Dimensions of the computational domain are $0 \le x \le 60$ and $0 \le y \le 40$ in the streamwise and transverse directions, respectively. Two cylinders with the same dimensionless radii

of 0.5 are virtually located at the transverse distance 10.75D from the inlet boundary. The Dirichlet boundary condition, $U_\infty = 1$ is imposed at the inlet boundary. The Neumann boundary condition of $\partial u/\partial y = 0$ is applied to the upper and lower boundaries. Another Neumann boundary condition of $\partial u/\partial x$ is imposed at the outlet boundary.

Two important parameters, dimensionless gap g^* and rotational speed α are varied to investigate their effects in this study. The magnitudes of g^* and α vary from 0 to 3. The direction of α is changed to result in either a decelerating or accelerating gap flow as shown in Figs. 1(a) and (b), respectively. The decelerating and accelerating gap flows yield diverging and converging vortex streets behind the cylinders respectively.

1. Mathematical Formulae and Numerical Method

Computational fluid dynamics research has, in recent times, gravitated around developing time efficient numerical methods with the capacity for handling complex geometries. The immersed boundary method has a proven capability for dealing with complex geometries and moving bodies. As a consequence of its use, the method eliminates both the need for conforming computational nodes to an exact boundary and for applying the adaptive grid generation in the case of moving objects (Noor et al., 2009). The immersed boundary method, which is based on Noor et al. (2009) previous work, is in principle, used to solve flow past two rotating circular cylinders in a side-by-side arrangement in the present exercise. As shall be apparent, a virtual force source term, distinct from that used in the original formulation of the method, is the backbone of the current skill.

2. Governing Equations

Defining the characteristic velocity and length, as the inlet velocity and diameter of a circular cylinder respectively, the non-dimensional governing equations for an incompressible viscous fluid can be written as follows:

$$\nabla . \mathbf{u} = 0, \tag{1}$$

and

$$\frac{\partial \mathbf{u}}{\partial t} + \nabla . (\mathbf{uu}) = -\nabla p + \frac{1}{\mathrm{Re}} \nabla^2 \mathbf{u} + \mathbf{f}. \tag{2}$$

The additional term on the RHS of Eq. (2), denoted by **f**, is the modified virtual force. It is included in Eq. (2) to accommodate the interaction between solids and fluids. To determine **f**, a new variable η is defined as the volume fraction of a solid in a computational cell. If a computational cell is filled with solid, then η is 1. On the other hand, η is 0 for a computational cell filled with fluid. η is a fraction between 0 and 1 for a cell partially filled with both fluid and solid. In this study, η is located at the center of a computational cell. It is determined by the distance between the center of a cell and the circular cylinder. Since the velocity of solid, $\mathbf{u_s}$, may not be equal to the velocity of fluid $\mathbf{u_f}$ in the same cell, the virtual force **f** is necessary to conserve the momentum in the cell according to Newton's second law and is then determined by

$$\mathbf{f} = \eta \frac{\mathbf{u_s} - \mathbf{u_f}}{\Delta t} \tag{3}$$

To cater for the rotating cylinder, $\mathbf{u_s}$ is prescribed as

$$\mathbf{u_s} = \frac{\Omega \times \mathbf{r}}{U_\infty} \tag{4}$$

where Ω is the angular speed, **r** is the distance between a point in the cylinder and the center of the cylinder and U_∞ is the inlet velocity.

3. Numerical Procedures

An in-house code based on Noor et al. (2009) previous work has been developed to solve Eqs. (1)-(4) by the following numerical procedures:

1. March the velocity vector field from the nth time level to the first intermediate level **u*** by solving Eq. (2) without the virtual force and pressure gradient. The second-order Adams-Bashford scheme is employed for the temporal derivative in Eq. (2). As a result,

$$\frac{\mathbf{u}^* - \mathbf{u}^n}{\Delta t} = S^n, \tag{5}$$

where

$$S^n = \frac{3}{2}\left(-\nabla \cdot (\mathbf{uu}) + \frac{1}{\mathrm{Re}} \nabla^2 \mathbf{u} \right)^n - \frac{1}{2}\left(-\nabla \cdot (\mathbf{uu}) + \frac{1}{\mathrm{Re}} \nabla^2 \mathbf{u} \right)^{n-1} \tag{6}$$

A staggered grid is applied to the established numerical model. The convective and diffusive terms are discretized using the third-order upwind and the central difference scheme, respectively.

2. March the velocity vector field from the first intermediate level **u*** to the second intermediate level **u**** by the SOLA algorithm proposed by Hirt et al. (1975). The SOLA algorithm iterates pressure and velocity to satisfy the continuity equation. When the mass residual in each cell is less than the predefined tolerance, **u**** and the pressure at the time level n+1 are obtained.
3. Update the virtual force **f** acting on each cell including solids by Eq. (3).
4. Update **u**** to the next time level $\mathbf{u}^{n+1}$ by

$$\mathbf{u}^{n+1} = \mathbf{u}^{**} + \Delta t \cdot \mathbf{f}^{n+1}. \tag{7}$$

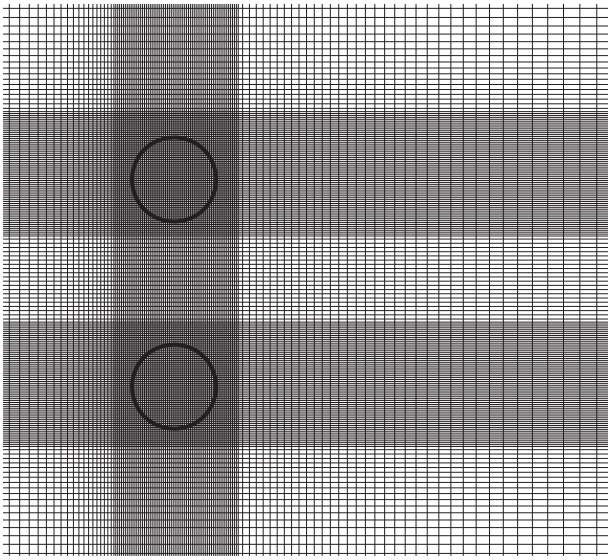

Fig. 2. Grid configuration near two cylinders for the case of g/D = 1.5.

5. The total virtual force **F** over the whole circular cylinder is calculated by

$$\mathbf{F} = \sum_{i=1}^{N} \mathbf{f}_i \Delta \forall_i, \tag{8}$$

where $\Delta \forall_i$ is the volume of a computational cell. Subsequently, the drag and lift coefficients can be determined by

$$C_L = -2 \cdot F_y \tag{9}$$

and

$$C_D = -2 \cdot F_x. \tag{10}$$

The computational time required to undertake a simulation is about 48 hours for each case with a mesh of 260 × 260 grids. The time increment Δt = 0.001 and the convergence criterion is of the order of 10^{-5} for the maximum mass residual are considered in this study. The CFL condition < 0.15 is chosen to determine the non-dimensional time step used in the present numerical model. The CPU and memory of the utilized PC cluster are AMD Athlon XP2600+ processor and 512 MB of RAM, respectively, while the CPU speed is 2 GHz.

Fig. 2 shows the typical grid distribution near the two cylinders for g/D = 1.5. A mesh size of 234 × 288 is used in the staggered grid arrangement. The fine grids are distributed in the vicinity of cylinders especially in the gap and the wake regions in order to accurately capture the separating shear layers around the cylinder and account for the high gradients near the surfaces. The mesh is coarser far from the cylinders. The distribution of grids within the cylinders is 66(x) × 66(y). To determine the effect of the variation of the gap spacing, the number of grids used in the y direction is tuned to maintain the

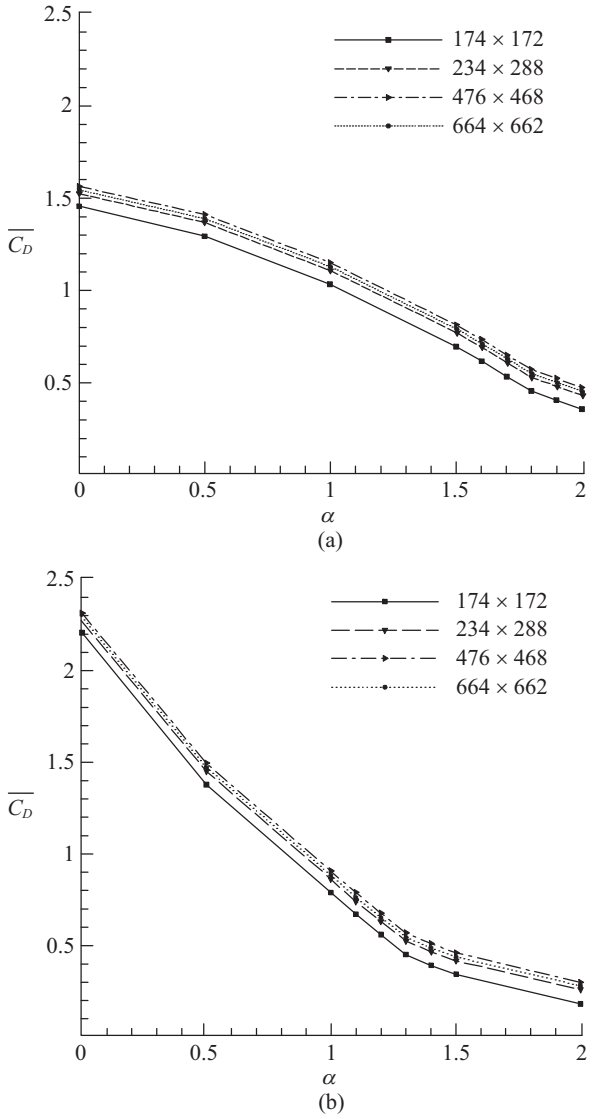

Fig. 3. Grid independence test in the cases of decelerating gap flow at g/D: (a) 3.0 and of (b) 0.2.

dense resolution near the cylinder and in the gap spacing. The grid refinement test has been carried out for the smallest gap of 0.2 and for the biggest gap of 3.0.

To ensure the computed results are independent of the grid size, several grid systems are considered for flow past two rotating circular cylinders in the case of decelerating gap flow cases at g^* = 3.0 and 0.2 as shown in Figs. 3(a) and (b), respectively. It is found that the mean value of the drag coefficient $\overline{C_D}$ increases with increase in the number of grids for both cases at g^* = 0.2 and 3. When the number of grids increase from 174 × 172 to 234 × 288, the value of $\overline{C_D}$ increases by about 5. When the number of grids further increases from 234 × 288 to 664 × 662, the value of C_D increases by about 2.5. Therefore, the mesh size 234 × 288 is considered appropriate for subsequent simulations.

Table 1. The comparison of average drag coefficients, recirculation length and Strouhal number at Re = 40 and Re = 100 in a single stationary cylinder.

	Re = 40		Re = 100		Method
	C_D	l_w	$\overline{C_D}$	S_t	
Roshko (1954)	-	-	-	0.160-0.170	Experiment
Tritton (1959)	1.480	-	1.25	-	Experiment
Pan (2006)	1.510	2.18	1.32	0.160	numerical method
Su et al. (2007)	1.630	-	1.40	0.168	numerical method
Tseng and Ferziger (2003)	1.530	2.21	1.42	0.164	numerical method
Chern et al. (2005)	1.480	2.20	-	-	numerical method
Dennis and Chang (1970)	1.522	2.35	-	-	numerical method
Dias and Majumdar (2002)	1.540	2.69	1.395	0.171	numerical method
Present study	1.570	2.22	1.38	0.170	numerical method

4. Validation of the Numerical Model

To validate the established numerical model, three benchmark problems have been performed. First, flow past a stationary circular cylinder at Re = 40 and 100 is considered. It is well known that at Re = 40, the wake behind the cylinder remains symmetric and a steady solution exists. Nevertheless, when Re exceeds 40, for example 100, the symmetry in the wake breaks and the flow becomes unsteady.

The comparisons of the drag coefficient, the recirculation length and the Strouhal number between the present numerical model and previous studies are presented in Table 1. For the flow at Re = 40, the drag coefficient $\overline{C_D}$ and the steady wake length l_w predicted by the proposed model are close to the results of previous studies. When the flow becomes unsteady at Re = 100, the predicted time averaged drag coefficient $\overline{C_D}$ and Strouhal number also agree with those of previous studies. Data in Table 1 confirms that the established model is able to predict flow past a stationary cylinder reasonably.

The second validation problem considers flow past a rotating circular cylinder at Re = 100. The direction of rotation is counter clockwise. To investigate the capability of the model for simulating flow past rotating cylinders in the main problem, the rotating angular velocity α of the circular cylinder is varied from 0 to 3. Table 2 shows variations of the time-averaged drag and lift coefficients, $\overline{C_D}$ and $\overline{C_L}$ with respect to α. The results are compared with numerical predictions by Yoon et al. (2009). $\overline{C_D}$ is inversely proportional to α, but $\overline{C_L}$ is proportional to α. Good agreements exist between numerical results predicted by Yoon et al. (2009) and the present model.

The two benchmark test results show that the established model is able to simulate the flow past a stationary or a rotating circular cylinder. Dynamic characteristics of the cylinder can be predicted reasonably well by the proposed model. Therefore, the numerical model is employed to simulate flow past a pair of side-by-side rotating cylinders.

Table 2. The comparison of time averaged drag and lift coefficients at Re = 100 in a rotating circular cylinder between the present model and Yoon et al. (2009).

α	Yoon et al. (2009)		Present study	
	$\overline{C_D}$	$\overline{C_L}$	$\overline{C_D}$	$\overline{C_L}$
0.0	1.305	0.023	1.381	0.015
0.5	1.253	-1.218	1.317	-1.234
1.0	1.122	-2.598	1.145	-2.544
1.5	0.835	-3.793	0.871	-3.970
2.0	0.479	-5.471	0.483	-5.540
3.0	0.216	-10.09	0.216	-10.12

III. RESULTS AND DISCUSSION

The flow past two rotating cylinders in a side-by-side arrangement either in a decelerating or accelerating gap flow is simulated at Re = 100 with varying rotational speeds and gaps. Fig. 1 shows rotating directions of two cylinders for a decelerating or accelerating gap flow. Influences of decelerating and accelerating gap flows on vortex streets and hydrodynamic forces exerted on the cylinders are demonstrated in the following.

1. Flow Pattern and Time History of Hydrodynamic Force

A distinction is made in the flow patterns arising from either a decelerating or accelerating gap ratio. Subsequently, a hydrodynamic force analysis is discussed.

1) Decelerating Gap Flow

When the upper and lower circular cylinders in a side-by-side arrangement rotate in the clockwise and counter clockwise directions respectively, the gap flow between these two circular cylinders is decelerated. Vortex shedding behind both cylinders incline toward the gap. To show the variation of vortex shedding with respect to varying rotational speed (α) and gap size (g^*), instantaneous vorticity contours and time

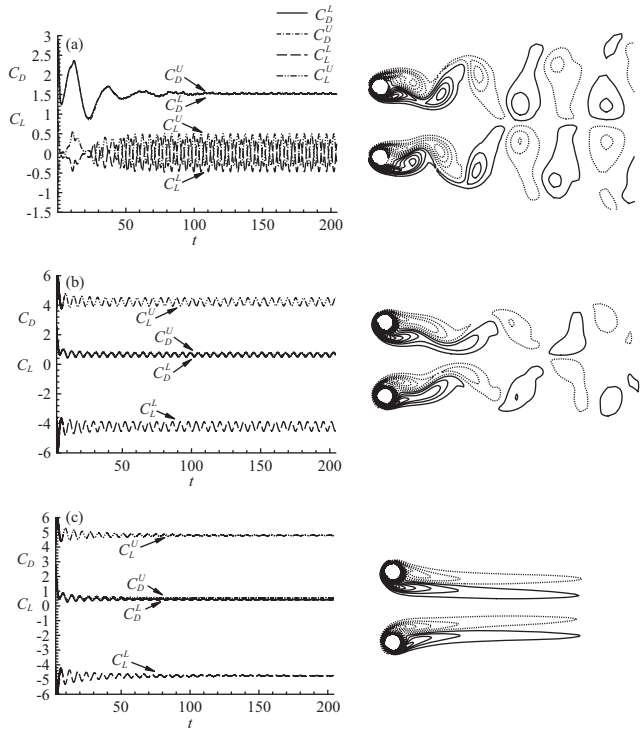

Fig. 4. Instantaneous vorticity contours (right column) at different speeds and the corresponding time histories of drag and lift coefficients (left column) in decelerating gap flow for g/D = 3.0 (a) α = 0 (b) α = 1.6 and (c) α = 1.8.

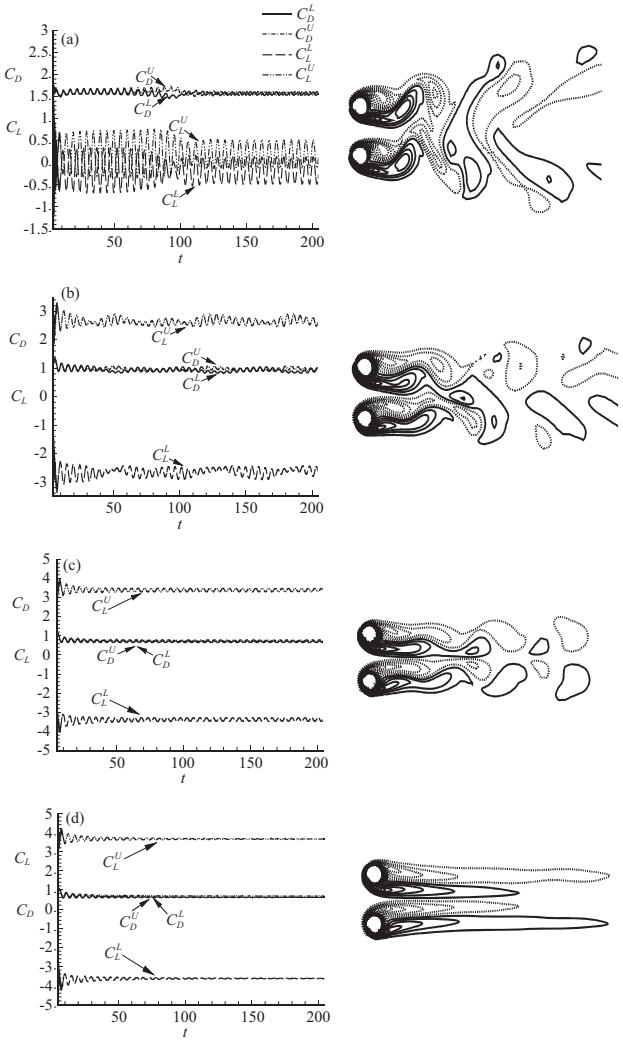

Fig. 5. Instantaneous vorticity contours (right column) at different speeds and the corresponding time histories of drag and lift coefficients (left column) in decelerating gap flow for g/D = 1.5 (a) α = 0 (b) α = 1.0 (c) α = 1.3 and (d) α = 1.4.

histories of drag and lift coefficients (C_D and C_L) are presented in Figs. 4-7. Fig. 4(a) shows time histories of drag and lift coefficients of two stationary cylinders at g^* = 3. Two vortex streets behind the cylinders maintain the anti-phase synchronized vortex shedding pattern which can also be found in the time history of C_L. The sinusoidal waveform of the lift coefficients indicates the periodic nature of vortex shedding behind the stationary cylinders. Also, the time averaged lift coefficients of the two stationary cylinders are almost zero just like for a uniform flow past a single stationary cylinder. Fig. 4(b) shows time histories of C_D and C_L for the rotating cylinders at α of 1.6. The anti-phase synchronized vortex shedding pattern is still found behind the two rotating cylinders. Nevertheless, it is also found that the time averaged lift coefficients are not zero any more due to the Magnus effect (Young et al., 2001). When α is increased to 1.8, vortex shedding behind the two cylinders is completely suppressed as shown in Fig. 4(c). Consequently, C_D and C_L reach steady states. The Magnus effect still exists in this case, so the time averaged lift coefficients of both cylinders are not zero but increased. The condition in which the vortex shedding is completely suppressed happens when α exceeds a critical value α_L. In this case with g^* of 3, α_L is 1.8.

To observe the effect of gap size, g^* is reduced from 3 to 1.5. Fig. 5(a) shows the flow pattern for two stationary cylinders. In the initial transition period before t = 80, the lift and drag coefficients of both cylinders are in anti-phase and in-phase modes, respectively. Eventually, these coefficients become anti-phase and in-phase after t = 100, respectively. The instantaneous vorticity contours at t = 350 shows that vortex shedding behind both cylinders synchronize with each other in the in-phase fashion just as soon as they shed from the cylinders. The vortices merge as they travel downstream. It is also found that the time averaged lift coefficients of both cylinders are not zero, although those cylinders do not rotate.

It is presumed that this is due to the narrow gap spacing of g^* = 1.5. When two cylinders rotate at α = 1, the time histories of lift and drag coefficients of both cylinders lose the regular periodicity but become modulated as shown in Fig. 5(b). Owing to the flip-flopping wake pattern behind the two cylinders as evident in Fig. 5(b), the respective drag coefficients are higher and lower in an alternating manner. When α increases to 1.3, it is found that the two vortices near the gap are strongly

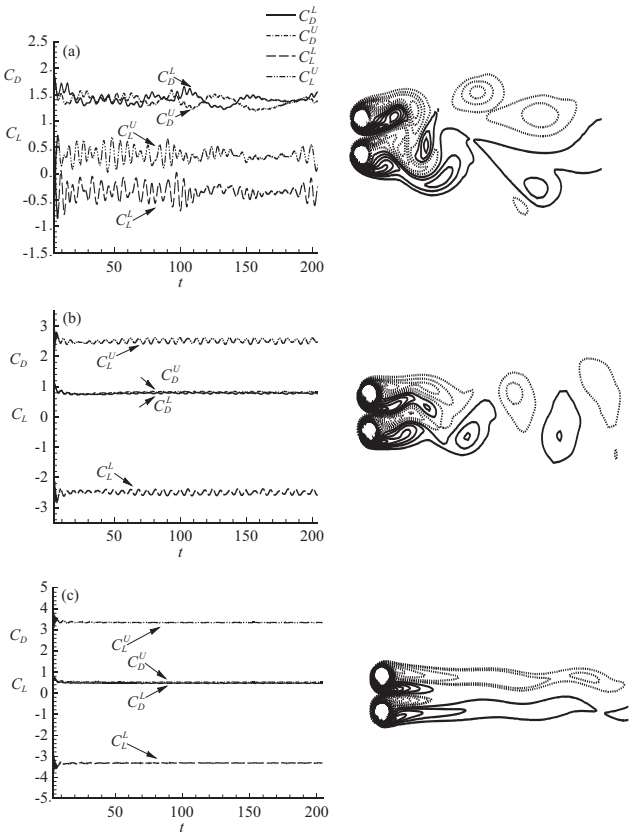

Fig. 6. Instantaneous vorticity contours (right column) at different speeds and the corresponding time histories of drag and lift coefficients (left column) in decelerating gap flow for g/D = 0.7 (a) α = 0 (b) α = 1.0 and (c) α = 1.4.

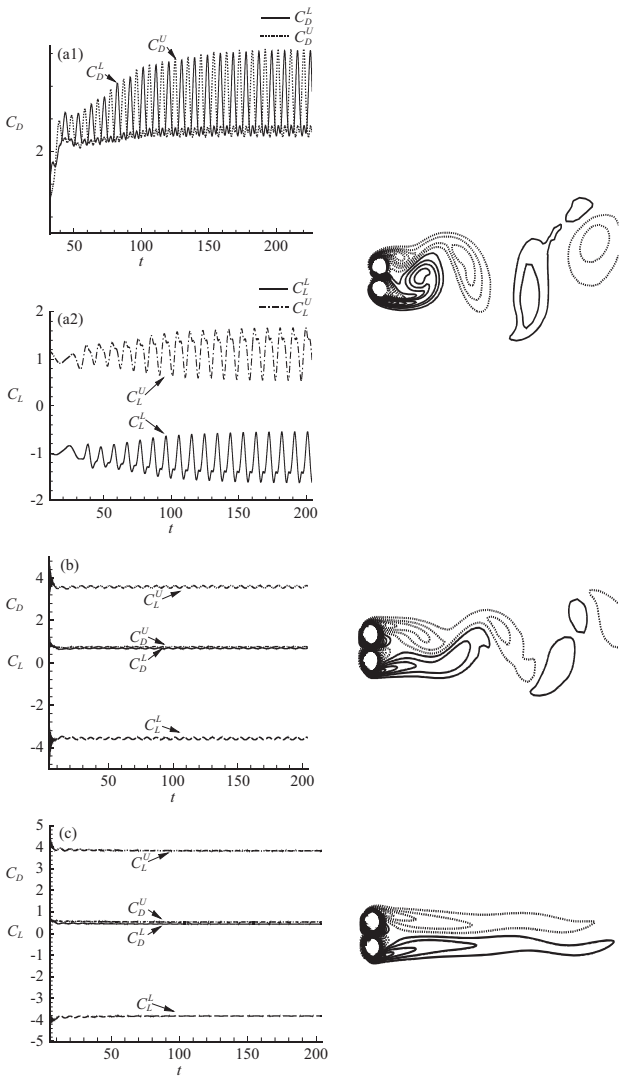

Fig. 7. Instantaneous vorticity contours (right column) at different speeds and the corresponding time histories of drag and lift coefficients (left column) in decelerating gap flow for g/D = 0.2 (a) α = 0 (b) α = 1.1 and (c) α = 1.3.

influenced by the gap flow. Vortex shedding behind the cylinders is still observed. The instantaneous vorticity contours in Fig. 5(c) show the anti-phase synchronized vortex shedding pattern accompanied by the drag coefficients of both cylinders. The anti-phased time traces of lift coefficients of both cylinders can be found in the time history of Fig. 5(c). Vortex shedding is suppressed when α reaches 1.4 as shown in Fig. 5(d). That is, α_L is 1.4 in this case. The wake behind the cylinders is stable and a steady state exists. Both C_D and C_L eventually remain constant. When both cylinders are close to each other and g^* = 0.7 as seen in Fig. 6(a), the characteristics of the flip-flopping wake pattern is observed behind the two stationary cylinders. This close proximity causes very complex behaviors of lift and drag coefficients in the time history displayed in Fig. 6(a).

In the case of α = 1, only a single vortex street behind the two cylinders exists as shown in Fig. 6(b). The two vortices adjacent to the gap are completely suppressed. Ultimately, the outer vortices govern the combined wake behind the two cylinders, resulting in a one-row vortex street. After the initial transient period, the lift coefficients of the cylinders are in in-phase mode. However, the drag coefficients of both are anti-phase according to Fig. 6(b). When α increases to 1.4, the vortex shedding in the near wake region is nearly suppressed, the outer vortices elongate far downstream, fluctuating very weakly at the downstream tail as shown in Fig. 6(c).

As g^* decreases to 0.2, only a single vortex street appears behind the two stationary cylinders as seen in Fig. 7(a). The flow structure keeps the single bluff-body wake pattern as shown in Fig. 7(a). Drag coefficients of both cylinders are in anti-phase mode. The waveform of the lift coefficients becomes irregular, meaning that nonlinearity in the flow becomes more obvious. When α is 1.1, the single vortex street still exists. Apparently, the expanding angle of the vortex street is decreased when two cylinders rotate at α = 1.1. Also, vortices are elongated. As α increases to 1.3, the vortices elongate and decrease in the lateral width. The vortex shedding is suppressed and the flow reaches a steady state as shown in Fig. 7(c).

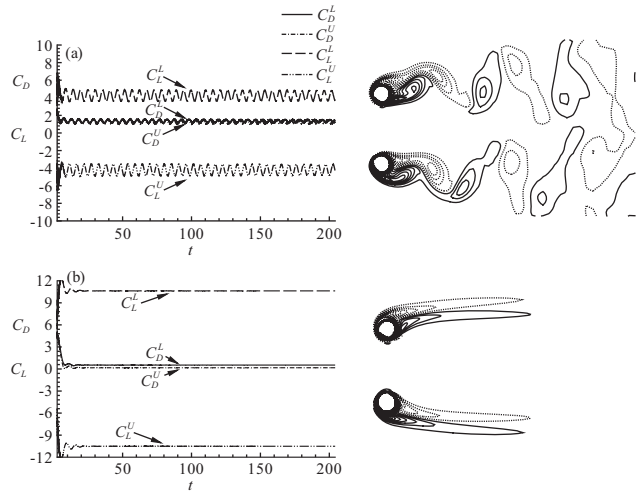

Fig. 8. Instantaneous vorticity contours (right column) at different speeds and the corresponding time histories of drag and lift coefficients (left column) in accelerating gap flow for g/D = 3.0 (a) α = 1.5 and (b) α = 3.0.

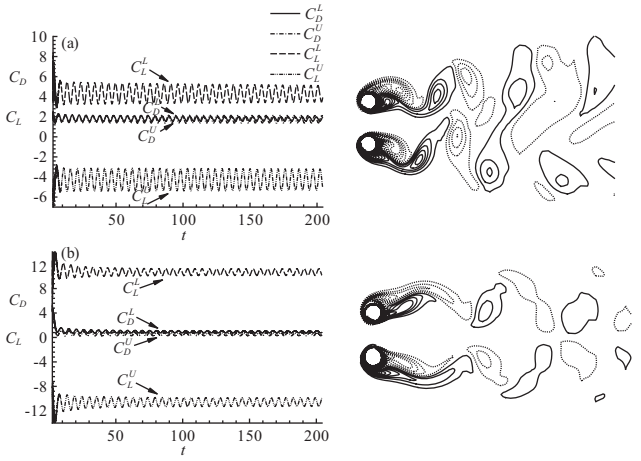

Fig. 9. Instantaneous vorticity contours (right column) at different speeds and the corresponding time histories of drag and lift coefficients (left column) in accelerating gap flow for g/D = 1.5 (a) α = 1.5 and (b) α = 3.0.

2) Accelerating Gap Flow

When the upper and lower cylinders rotate in the counter clockwise and clockwise directions respectively, the gap flow between them is accelerated. Vortices shed behind the cylinders are deflected far away from each other as they travel downstream. Fig. 8 shows instantaneous vorticity contours and corresponding time histories of drag and lift coefficients at a large gap ratio of g^* = 3. In the stationary case, vortex shedding behind the cylinders behaves in an anti-phase mode as shown in Fig. 4(a). When the cylinders begin to rotate at α = 1.5, the vortex shedding behind them change to an in-phase pattern. The in-phase behavior can also be found in time histories of lift coefficients. In addition to this, the expanding angle of the vortex shedding is increased as vortices travel downstream. Fig. 8(b) shows the flow pattern for two very fast rotating cylinders at α of 3. Vortex shedding is completely suppressed in this case. The stable fashion of the dynamic forces is shown in Fig. 8(b).

Fig. 5 shows the flow pattern and time histories of two stationary cylinders, when the gap is reduced to 1.5. It has already been mentioned that vortex shedding behind cylinders is in anti-phase at the beginning of the simulation for stationary cylinders. After t = 100, in-phase vortex shedding is found. In cases with a decelerating gap flow, vortex shedding is suppressed when α > 1.4. However, in the case with an accelerating gap flow at α = 1.5, vortex shedding still exists as shown in Fig. 9(a). The in-phase synchronized flow pattern is observed. Vortices shedding from rotating cylinders merge soon after they leave the cylinders. The in-phase feature can also be found in time histories of C_L of the cylinders as shown in Fig. 9(a). The vortex shedding is not suppressed even when α reaches 3. In Fig. 9(b), vortex shedding behaves in an anti-phase manner and time histories of the lift coefficient also shows the anti-phase feature. The drag coefficient of the lower cylinder is slightly higher than that of the upper cylinder.

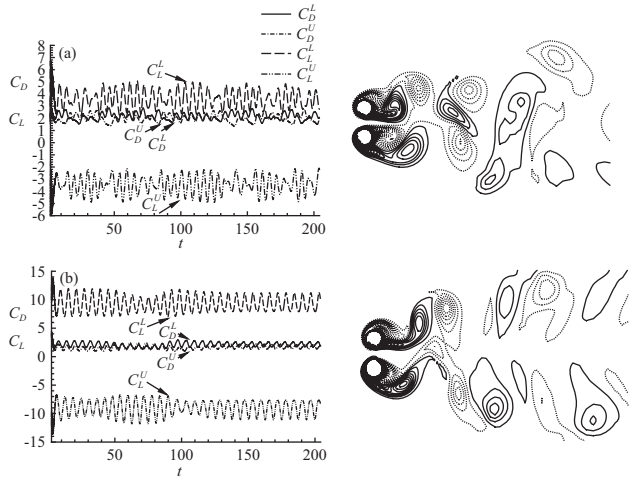

Fig. 10. Instantaneous vorticity contours (right column) at different speeds and corresponding time histories of drag and lift coefficients (left column) in accelerating gap flow cases for g/D = 0.7 (a) α = 1.5 and (b) α = 3.0.

When both cylinders are placed at g^* = 0.7, for the stationary case, vortex shedding behaves in a flip-flopping pattern in which two distinctive vortex streets are formed. One wide and the other narrow one are found behind the lower and upper cylinders as shown in Fig. 6(a) respectively. When both cylinders rotate at α = 1.5, the flip-flopping pattern appears downstream. The drag coefficient on one side of the cylinder is higher than that of the other side in an alternating way, reflecting the strength of the flip-flopping wake pattern as shown in Fig. 10(a). As α increases to 3, vortex shedding exhibits the in-phase pattern which is also found in the time history of the lift coefficients in Fig. 10(b).

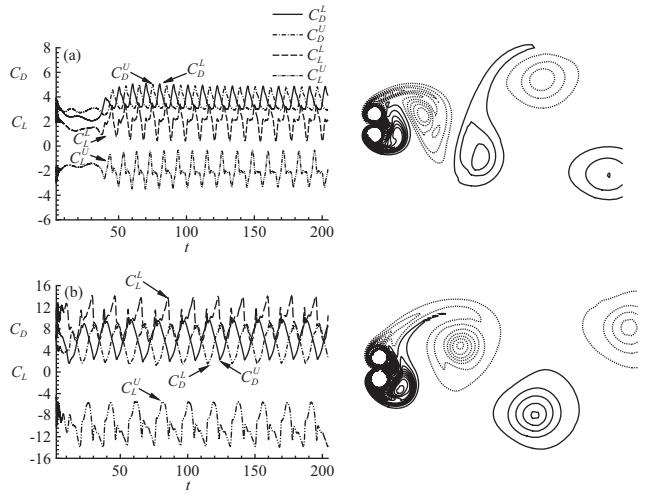

Fig. 11. Instantaneous vorticity contours (right column) at different speeds and the corresponding time histories of drag and lift coefficients (left column) in accelerating gap flow cases for g/D = 0.2 (a) α = 1.5 and (b) α = 3.0.

When both stationary cylinders are placed in a very narrow gap of g^* = 0.2, only a single vortex street is found (Fig. 7). While the vortices adjacent to the gap do not evolve in the vortex street any more, the vortex shedding is mainly governed by the interaction of the outer vortices from both cylinders. As α increases to 1.5, the size of vortices increase in the lateral width. Increase of the lateral width is also found in the case of α = 3. Vortex shedding largely grows as α increases. When α increases from 1.5 to 3, the expanding angle of developing vortex shedding along the downstream direction increases from 80° to 120° as shown in Figs. 11(a) and (b), respectively. The amplitudes of lift and drag coefficients strongly fluctuate as α increases (see Figs. 11(a) and (b)). Irregular waveforms are found in time histories of lift coefficients. In summary, for the cases with an accelerating gap flow, vortex shedding cannot be suppressed in the range of rotational speeds 0 to 3.0, except for the case of the large gap spacing of 3 and at the fast rotating speed of 3.

2. Drag and Lift Coefficients

As has been done previously a distinction between the decelerating and accelerating gap flow drag and lift coefficient results is considered.

1) Decelerating Gap Flow

In order to explore variations of hydrodynamic forces exerted on the two cylinders, lift and drag coefficients are calculated. Figs. 12(a) and (b) show variations of the time averaged drag and lift coefficients ($\overline{C_D}$ and $\overline{C_L}$) for cases with a decelerating gap flow with respect to α and g^*. Drag coefficients of the two cylinders are very close, so only the drag coefficient of the upper cylinder is displayed. It is found that $\overline{C_D}$ decreases when α increases as shown in Fig. 12(a). This

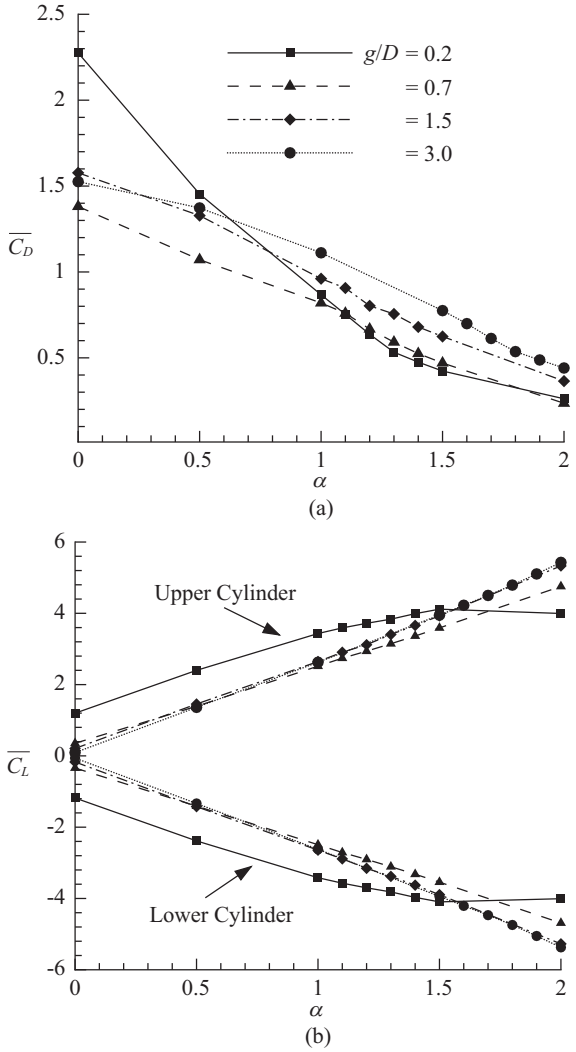

Fig. 12. Time averaged drag and lift coefficients ($\overline{C_D}$ and $\overline{C_L}$) of decelerating gap flow cases (a) $\overline{C_D}$ and (b) $\overline{C_L}$.

tendency is also found in results of a free stream past a single rotating cylinder, which were provided by Kang and Choi (1999), Stojkovic et al. (2002) and Mittal and Kumar (2003). When the gap is reduced from 3 to 0.7, $\overline{C_D}$ decreases. Nevertheless, an interesting behavior of $\overline{C_D}$ is found in the case of g^* = 0.2. When the cylinders are stationary, $\overline{C_D}$ for g^* = 0.2 is larger than that with a bigger gap. However, when α varies from 1 to 2, $\overline{C_D}$ for g^* = 0.2 rapidly drops and is less than that with a bigger gap.

Fig. 12(b) shows variations of $\overline{C_L}$ with respect to α and g^*. In the cases of g^* = 3, 1.5 and 0.7, $\overline{C_L}$ is proportional to α due to the Magnus effect. The repulsive force between two cylinders results in a higher pressure on the gap side surfaces of both cylinders compared to that on the opposite side surfaces. Consequently, the positive and negative mean lift forces

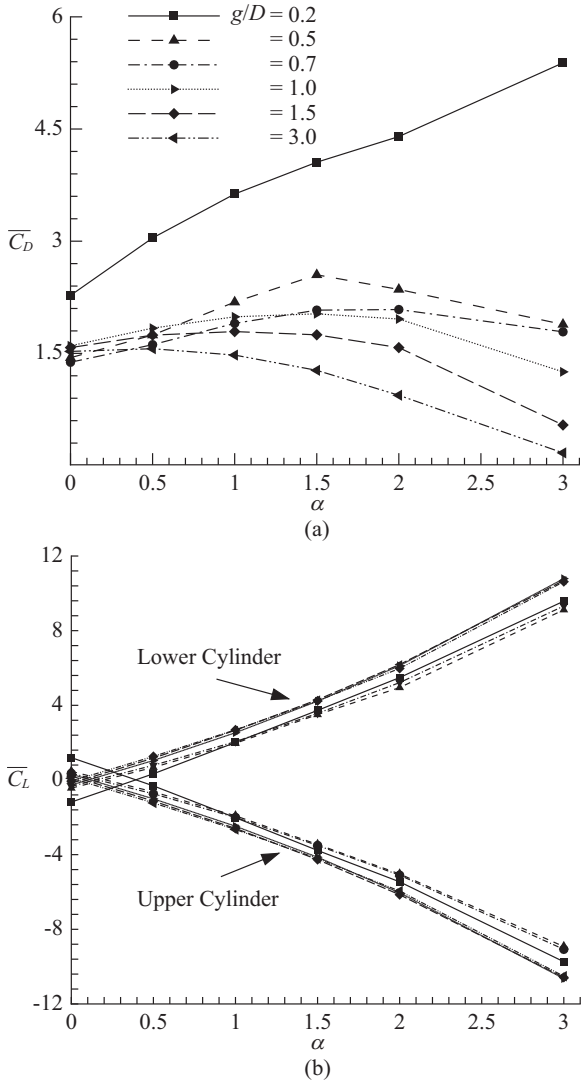

Fig. 13. Time averaged drag and lift coefficients ($\overline{C_D}$ and $\overline{C_L}$) of accelerating gap flow cases (a) $\overline{C_D}$ and (b) $\overline{C_L}$.

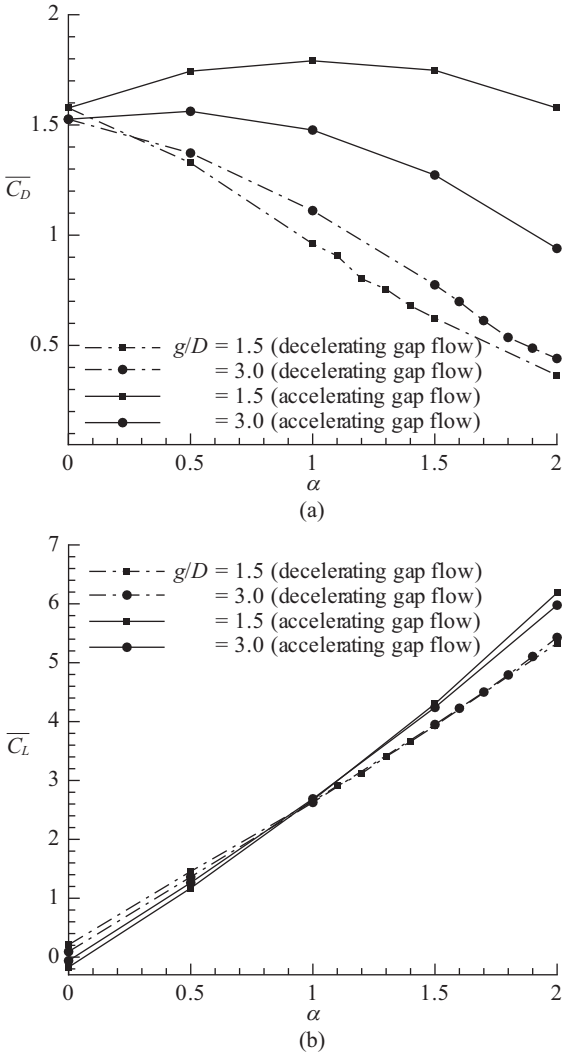

Fig. 14. Comparison of decelerating and accelerating gap cases (a) Time averaged drag coefficients ($\overline{C_D}$) and (b) Time averaged lift coefficients ($\overline{C_L}$).

are exerted on the upper and lower cylinders, respectively. Another interesting case is found when $g^* = 0.2$. When $\alpha > 1.5$, the $\overline{C_L}$ curve is almost horizontal.

2) Accelerating Gap Flow

In cases with an accelerating gap flow, Figs. 13(a) and (b) show variations of $\overline{C_D}$ and $\overline{C_L}$ with respect to varying α and g^*. For cases of g^* varying from 3.0 to 0.5, $\overline{C_D}$ is proportional to α and then inversely proportional to α. In other words, there is a maximum for each curve of $\overline{C_D}$. For the case of $g^* = 0.2$, $\overline{C_D}$ is proportional to α. Furthermore, the characteristics of C_L have the same tendency as for the cases with a decelerating gap flow showing that $\overline{C_L}$ is proportional to α (Fig. 12(b)).

3. Comparison between Decelerating and Accelerating Gap Flows

Figs. 14(a) and (b) show the comparison of $\overline{C_D}$ and $\overline{C_L}$ for cases with a decelerating or accelerating gap flow. It is found that the drag coefficients of the cases with an accelerating gap flow are higher than those of the cases with a decelerating gap flow. It may be because vortex shedding can be completely suppressed in cases with a decelerating gap flow and the wake behind cylinders becomes narrower. However, in the cases with an accelerating gap flow, vortex shedding cannot be completely suppressed except for the case of $g^* = 3$.

It is observed that $\overline{C_L}$ is proportional to α for cases with a decelerating or accelerating gap flow. When α is less than 1, $\overline{C_L}$ of the cases with a decelerated gap flow is higher than those in cases with an accelerating gap flow as shown in Fig.

14(b). Vortex shedding is incline towards each other before being finally suppressed at very fast α. Nevertheless, in the case of an accelerating gap flow, vortex shedding is inclined far away from each other. However, when $\alpha > 1$, $\overline{C_L}$ in the cases with an accelerating gap flow is higher than in the decelerating gap flow. This may be because no interaction between two vortex shedding occurs in the cases with decelerating gap flows and vortex shedding is completely suppressed at fast α. In the cases with an accelerating gap flow, the interaction of vortex shedding between both cylinders still exists and influences the repulsive force between cylinders.

4. Autocorrelation Function

In order to determine the level of the relationship between the two vortex streets behind the upper and lower cylinders, Chern et al. (2005) proposed the autocorrelation function. The autocorrelation $A(T)$ can be calculated by Eqs. (11) and (12) denoted as

$$A(T) = \frac{\overline{C_L^U C_L^L}}{\overline{C_L^{U^2}}}, \tag{11}$$

where

$$\overline{C_L^U C_L^L} = \lim \frac{1}{T_f - T_i} \int_{T_i}^{T_f} C_L^U(t) C_L^L(t) dt. \tag{12}$$

The superscripts L and U refer to the lower and upper cylinders, respectively. T_i and T_f represent the initial time and final time, respectively. The lift coefficient is employed in the $A(T)$ because it is strongly affected by vortex shedding. Therefore, C_L can respond to the variation of vortex shedding. As long as C_L^U is equal to C_L^L, $A(T)$ is 1. This state corresponds to an in-phase mode. Moreover, $A(T)$ becomes -1 when C_L^U and C_L^L are equal in magnitude but of opposite signs. Hence, C_L^U and C_L^L are in anti-phase. If C_L^U is completely unrelated to C_L^L, then $A(T)$ is zero. In addition, $A(T)$ varies from 0 to 1 and 0 to -1 when C_L^U is partially related to C_L^L either in in-phase or anti-phase, respectively. Thus, $A(T)$ can be used to examine the degree of interaction between the vortex systems behind the two cylinders.

1) Decelerating Gap Flow

Figs. 15 and 16 present the time histories of $A(t)$ for the cases with decelerating and accelerating gap flows, respectively. $A(t)$ remains -1 when $g^* = 3$ and $\alpha < 1.8$ (see Fig. 15(a)). This outcome conforms to results seen in Figs. 4(a) and (b). This means that an anti-phase mode exists in vortex shedding when a decelerating gap flow occurs. When $\alpha = 1.8$, vortex shedding is suppressed. The lift coefficients of both cylinders are zero, so α is zero as well. Considering an intermediate gap of 1.5, α for the two stationary cylinders ($\alpha = 0$) varies from -1 to 1 (Fig. 15(b)). This shows that vortex shedding shifts from

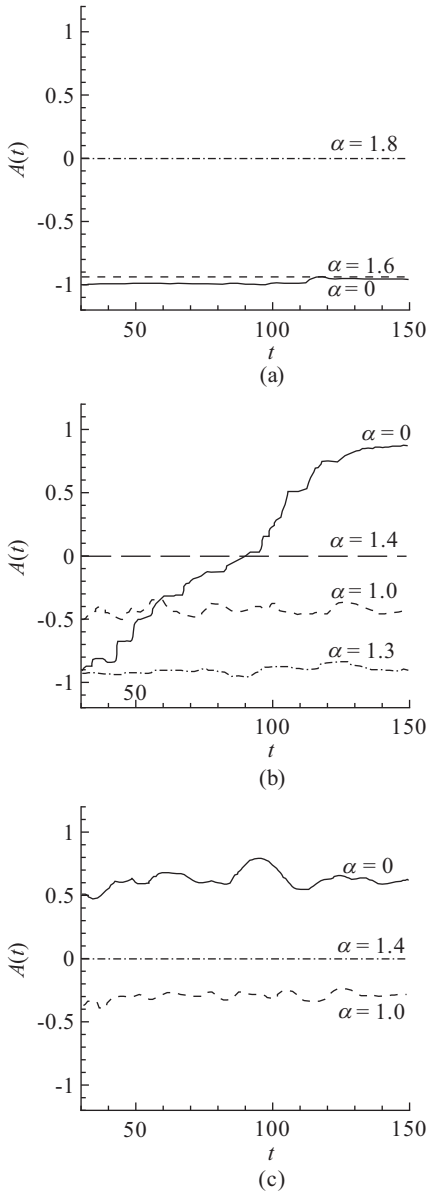

Fig. 15. Time histories of autocorrelation function $A(t)$ in the decelerating gap flow cases for g/D (a) 3.0, (b) 1.5 and (c) 0.7.

the anti-phase mode to the in-phase mode. As α increases to 1.0, the average value of $A(t)$ is about -0.5 as shown in Fig. 15(b). This result gives the information that the interaction between vortex systems are in partial anti-phase. When α gradually increases to 1.3, $A(T)$ is about -0.9.

Vortex shedding is in anti-phase synchronized pattern in this case. Finally, vortex shedding is suppressed and $A(T)$ is zero as well as α being 1.4, i.e. there is no interaction between the vortex systems.

As the gap between the cylinders is reduced further, Fig. 15(c) shows variation of $A(T)$ in the cases with different rotating speeds. In the case of stationary cylinders, $A(T)$ fluctuates around 0.5, indicating that the interaction of vortex shedding is in a partially in-phase synchronized pattern. When

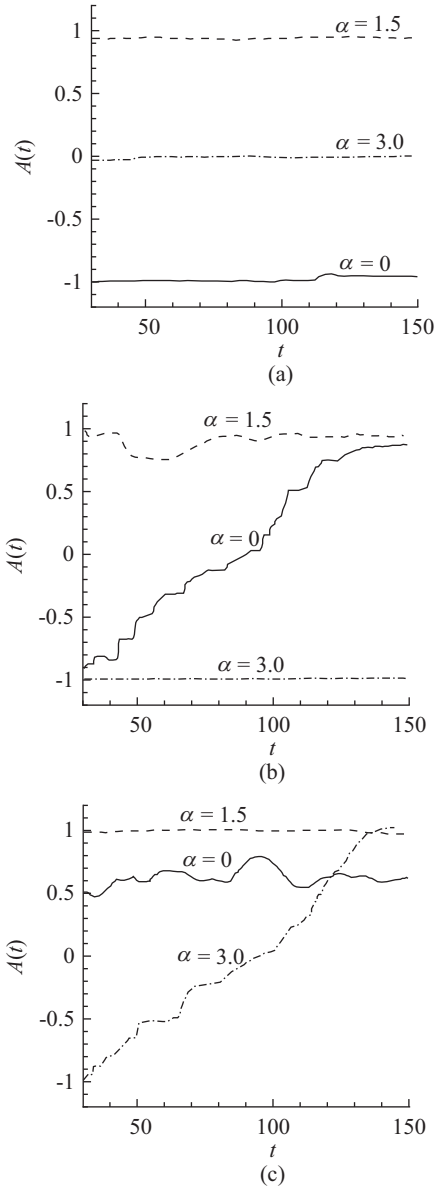

Fig. 16. Time histories of autocorrelation function $A(t)$ in the decelerating gap flow cases for g/D (a) 3.0, (b) 1.5 and (c) 0.7.

the two cylinders start to rotate at $\alpha = 1$, $A(T)$ becomes negative. This refers to a partial anti-phase mode in vortex shedding. Also, when α reaches 1.4, vortex shedding is suppressed, so $A(T)$ is zero again.

2) Accelerating Gap Flow

Fig. 16 presents the time histories of $A(T)$ in the cases with accelerating gap flows. For $g^* = 3$, when the cylinders start to rotate at $\alpha = 1.5$, $A(T)$ is almost 1 as shown in Fig. 16(a), meaning that vortex shedding behaves in-phase shedding pattern (Fig. 8(a)). As α increases to 3.0 $A(T)$ is close to zero in Fig. 16(a). In this case, vortex shedding is completely suppressed.

By reducing the gap to 1.5, for stationary cases, $A(T)$ shows the transitional pattern from -1 to 1 as shown in Fig. 16(b). It indicates in this regime vortex shedding shifts from the anti-phase to the in-phase synchronized pattern. When the cylinders begin to rotate at $\alpha = 1.5$, $A(T)$ is almost 1. In this case, vortex shedding of both cylinders shows the in-phase pattern. As α increases to 3.0 the average value of $A(T)$ is -1, as shown in Fig. 16(b). Vortex shedding in this regimes remains in the anti-phase synchronized pattern.

When the gap reduces to 0.7, for the stationary case, $A(T)$ is in the fractional value of 0.5 as shown in Fig. 16(c). This indicates that vortex shedding is partially related to the in-phase pattern. When the cylinders start to rotate at $\alpha = 1.5$, the value of $A(T)$ is 1. This means that vortex shedding remains in the in-phase pattern. As α increases to 3.0, $A(T)$ shows the transitional pattern from -1 to 1, showing that in this regime, vortex shedding shifts from the anti-phase to the in-phase synchronized pattern.

IV. CONCLUSIONS

The present study has numerically investigated the characteristics of a uniform flow past two counter rotating circular cylinders in a side-by-side arrangement at various rotational speeds (α). The direction of rotation results in decelerating and accelerating gap flows. The immersed-boundary method is adopted to handle the simulation of two counter rotating circular cylinders in the Cartesian coordinates.

The established model has been validated by the simulation of a uniform flow past a stationary circular cylinder. Subsequently, the proposed immersed boundary model is applied to simulations of cases with a decelerating and accelerating gap flow. Two vortex shedding modes (in-phase and anti-phase) are found behind the two cylinders. It is found that vortex shedding is suppressed as the cylinders rotate very fast.

ACKNOWLEDGMENTS

The authors would like to express their gratitude for the financial support from Ministry of Science and Technology of Taiwan (No: MOST 103-2221-E-011-110-MY3).

REFERENCES

Bearman, P. W. and A. J. Weadcock (1973). The interaction between a pair of a circular cylinders normal to a stream. Journal of Fluid Mechanics 61, 499-511.

Chern, M. J., A. G. L. Borthwick and R. Eatock Taylor (2005). Pseudospectral element model for free surface viscous flows. International Journal for Numerical Methods in Fluids 15, 517-554.

Dennis, S. C. R. and G. Z. Chang (1970). Numerical solutions for steady flow past a circular cylinder at Reynolds numbers up to 100. Journal of Fluid Mechanics 42, 471-489.

Dias, A. and S. Majumdar (2002). Numerical computation of flow around a circular cylinder. Technical Report, PS II Report, BITS Pilani, India.

Guo, X. H., J. Z. Lin, C. X. Tu and H. L. Wang (2009). Flow past two rotating circular cylinders in a side-by-side arrangement. Journal of Hydrodynamics 21, 143-151.

Hirt, C. W., B. D. Nichols and N. C. Romero (1975). Sola - a numerical

solution algorithm for transient fluid flow. LA-5852 technical report.

Kang, S. (2003). Characteristics of flow over two circular cylinders in a side-by-side arrangement at low Reynolds numbers. Journal of Fluids and Structures 15, 2486-2498.

Kang, S. M. and H. C. Choi (1999). Laminar flow past a rotating circular cylinder. Physics of Fluids 11, 3312-3319.

Meneghini, J. R., F. Saltara, C. L. R. Siqueira and J. J. Ferrari (2001). Numerical simulation of flow in interference between two circular cylinders in tandem and side-by-side arrangements. Journal of Fluids and Structures 15, 327-350.

Mittal, S. and B. Kumar (2003). Flow past a rotating cylinder. Journal of Fluid Mechanics 476, 303-334.

Noor, D. Z., M. J. Chern and T. L. Horng (2009). An immersed boundary method to solve fluid-solid interaction. Computational Mechanics 44, 447-453.

Pan, D. (2006). An immersed boundary method on unstructured cartesian meshes for incompressible flow with heat transfer. Numerical Heat Transfer Part B 49, 277-297.

Roshko, A. (1954). On the drag and shedding frequency of two dimensional bluff bodies. Technical Note, National Advisory Committee for Aeronautics (NACA), Washington 3169.

Stojkovic, D., M. Breuer and F. Durst (2002). Effect of high rotation rates on the laminar flow around a circular cylinder. Physics of Fluids 14, 3160-3178.

Su, S. W., M. Lai and C. A. Lin (2007). An immersed boundary technique for simulating complex flows with rigid boundary. Computers and Fluids 36, 313-324.

Tritton, D. J. (1959). Experiments on the flow past a circular cylinder at low Reynolds number. Journal of Fluid Mechanics 6, 547.

Tseng, Y. H. and J. H. Ferziger (2003). A ghost-cell immersed boundary method for flow in complex geometry. Journal of Computational Physics 192, 593-623.

Yoon, H. S., H. H. Chun, J. H. Kim and I. L. R. Park (2009). Flow characteristics of two rotating side-by-side circular cylinders. Computers and Fluids 38, 466-474.

Young, D. F., B. R. Munson and T. H. Okiishi (2001). A Brief Introduction of Fluid Mechanics, 2nd Edition. John Wiley & Sons, New Jersy, USA.

Zdravkovich, M. M. (1982). Flow induced oscillations of two interfering circular cylinders. Journal of Sound and Vibration 101, 511-521.